Letter

Extracting off-diagonal order from diagonal basis measurements

Bo Xiao [1,*] Javier Robledo Moreno [1,2,†] Matthew Fishman,[1] Dries Sels,[1,2] Ehsan Khatami [3] and Richard Scalettar[4]

[1]*Center for Computational Quantum Physics, Flatiron Institute, 162 Fifth Avenue, New York, New York 10010, USA*

[2]*Department of Physics, New York University, New York, New York 10003, USA*

[3]*Department of Physics and Astronomy, San José State University, San José, California 95192, USA*

[4]*Department of Physics and Astronomy, University of California, Davis, California 95616, USA*

(Received 14 October 2022; revised 11 November 2023; accepted 28 March 2024; published 17 June 2024)

Quantum gas microscopy has developed into a powerful tool to explore strongly correlated quantum systems. However, discerning phases with topological or off-diagonal long range order requires the ability to extract these correlations from site-resolved measurements. Here, we show that a multiscale complexity measure can pinpoint the transition to and from the bond ordered wave phase of the one-dimensional extended Hubbard model with an off-diagonal order parameter, sandwiched between diagonal charge and spin density wave phases, using only diagonal descriptors. We study the model directly in the thermodynamic limit using the recently developed variational uniform matrix product states algorithm, and draw our samples from degenerate ground states related by global spin rotations, emulating the projective measurements that are accessible in experiments. Our results will have important implications for the study of exotic phases using optical lattice experiments.

DOI: 10.1103/PhysRevResearch.6.L022064

Introduction. Quantum gas microscopy for ultracold atoms in optical lattices, in which high-resolution real-space snapshots of the many-body system are accessible, is a prominent tool for studying strongly correlated systems [1–3]. These projective measurements can be analyzed "by hand" with traditional counting to compute observables, both local or extended spin and charge correlations [4–8]. The snapshots are often termed "diagonal" since they comprise measurements of density observables $n_{i\sigma} = \langle c^\dagger_{i\sigma} c_{i\sigma} \rangle$, where $c^\dagger_{i\sigma}$ ($c_{i\sigma}$) is the spin-σ fermion creation (destruction) operator at site i, which have matching row and column indices of the Greens function G^σ_{ii}.

The same is true for the outcome of large-scale programmable quantum simulators based on Rydberg atoms, which allow arranging a large number of qubits in arbitrary lattice geometries and controlling the Hamiltonian evolution of the system [9–15]. A crucial open question is whether the fact that these experiments do not at present capture "off-diagonal" information encoded in the full G^σ_{ij} will limit the insight they can yield.

Recent advances in machine learning methods [16–18] hold promise for answering this question. Convolutional neural networks and hybrid supervised-unsupervised approaches have been used to classify quantum gas microscopy data in emulations of the two-dimensional Fermi-Hubbard model [19], to visualize and identify multiparticle diagonal correlations [20,21], and to detect new diagonal ordered phases in Rydberg atom quantum simulators [22]. Momentum-space images of cold atoms have also been analyzed to identify quantum phase transitions [23,24].

Machine learning methods are able to capture order parameters or relevant thermodynamic quantities in classical as well as quantum systems, and therefore detect symmetry-breaking phases [25–32]. In contrast, it is much harder to identify topological phase transitions involving off-diagonal long range order. In the realm of classical statistical physics, the two-dimensional XY and q-state clock models have been investigated to identify Berenzinskii-Kosterlitz-Thouless (BKT) transitions [33–35]. However, much less is known for BKT-type quantum phase transitions.

The simplest context in which this issue can be explored is that of quasi-one-dimensional materials, e.g., organic conductors, carbon nanotubes [37–41], for which the one-dimensional extended Hubbard model is a minimal description [42–47]:

$$H = -t \sum_{i,\sigma} (c^\dagger_{i,\sigma} c_{i+1,\sigma} + c^\dagger_{i+1,\sigma} c_{i,\sigma}) + U \sum_i n_{i,\uparrow} n_{i,\downarrow} + V \sum_{i,\sigma\sigma'} n_{i,\sigma} n_{i+1,\sigma'}, \quad (1)$$

where U and V are on-site and nearest-neighbor Coulomb interactions and $t = 1$ sets the unit of energy. An infinitesimally small U drives a transition to a regime with quasilong range spin order [47]. We will refer to this as a "SDW," but emphasize that the ground state spin correlations decay as a power law. Similarly, an infinitesimally small V induces charge density wave (CDW) order with staggered empty and doubly occupied sites [47]. However, much less obvious is the

*Present address: Quantum Science Center, Oak Ridge National Laboratory, Oak Ridge, Tennessee 37831, USA; bxiao@flatironinstitute.org

†jrm874@nyu.edu

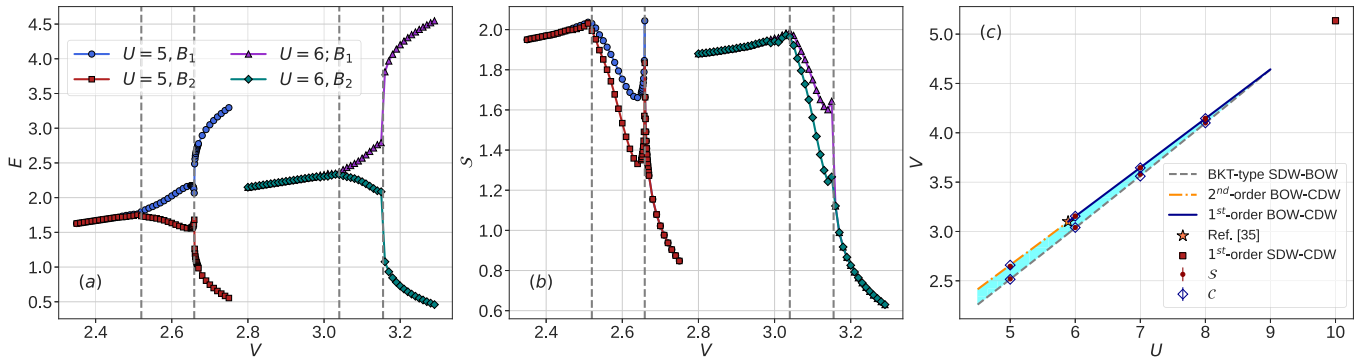

FIG. 1. (a) Energy E_i on two bonds $B_i (i = 1, 2)$ associated with one two-site unit cell and (b) von Neumann entanglement entropy $\mathcal{S}_i$ computed via partitioning along these two bonds vs nearest-neighbor interaction V at fixed $U = 5$ and $U = 6$. (c) Phase diagram of the one-dimensional extended Hubbard model at half filling in the U-V plane. Phase boundaries are determined using the structural complexity $\mathcal{C}$ (blue diamond) and corroborated by the entanglement entropy $\mathcal{S}$ (red circle) at select U's. The blue shaded region denotes the BOW phase which is characterized by off-diagonal long-range order. The orange star indicates a tricritical point where the nature of BOW-CDW transition switches from second order to first order, based on Ref [36]. The red square indicates a direct first-order transition from SDW to CDW at $U = 10$, determined using the structural complexity $\mathcal{C}$. Bond dimension $\mathcal{D} = 2000$ is employed.

existence, between these two phases, of a narrow bond ordered wave (BOW) region with alternating large and small kinetic energy on adjacent sites, and a BKT-type transition separating it from the SDW phase [36,45,48–53] [see Fig. 1(c)]. Converged results on the exact location of this BKT-type transition have not been obtained [54–57]. The model thus offers a unique opportunity to test machine learning tools for examining subtle quantum phase transitions characterized by nondiagonal order.

In this paper, we use the state-of-the-art variational uniform matrix product states (VUMPS) algorithm [58–60] to obtain the ground state of the model at half filling, directly in the thermodynamic limit (TDL). We then emulate projective and diagonal measurements on optical lattice experiments by sampling spin-resolved occupancy snapshots from the VUMPS wavefunction. These snapshots are first analyzed using principal component analysis (PCA), and then using a recently proposed structural complexity measure [61,62]. We find that while PCA accurately captures the first and second order transitions between the BOW and CDW phases and the associated CDW order parameter, it fails to identify differences between the SDW and BOW samples. The structural complexity, on the other hand, starts off with a long bitstring consisting of concatenated samples, and through a series of coarse-graining steps is able to deduce the location of both transitions.

Variational Uniform Matrix Product States. Inspired by tangent space ideas [58,63,64], VUMPS optimizes a translational invariant matrix product state (MPS) directly in the TDL, in contrast to the more traditional infinite size density matrix renormalization group (iDMRG) [65–67] algorithm which starts from a small system and grows the state one site at a time.

Similar to DMRG, the energy minimization problem is reformulated as a series of local eigenvalue problems of effective Hamiltonians projected into the MPS basis. In practice a linear solver is used to perform the sum of the formally infinite number of Hamiltonian terms to obtain the effective Hamiltonians. By working directly with a translational invariant ansatz in VUMPS, we can remove the solitonic excitation induced by the use of open boundary conditions [55,57]. In practice, all of our VUMPS calculations of the extended Hubbard model use a single-site update with a two-site unit cell, and we constrain our states to conserve $U(1)$ particle number and spin projection symmetry [59,68]. We also constrain our states to be in the $S_z = 0$ symmetry sector. Results of convergence with bond dimension are shown in Supplemental Material [69].

Figure 1(a) shows the energy E on two bonds B_i $(i = 1, 2)$ that are associated with a two-site unit cell, computed using VUMPS. It shows clear signals of both phase transitions. For each fixed U, energies E_1 and E_2 inside one unit cell are exactly equal to each other in the SDW phase when V is small. As V is gradually increased, E_1 and E_2 split, which reflects the broken translational symmetry of the BOW phase. The phase boundary between SDW and BOW can be determined quantitatively by setting a small threshold, e.g., where $|E_1 - E_2| \sim 10^{-5}$. As V is further increased, the smooth or sudden changes in the energy per bond characterize the second-order $(U = 5)$ or first-order $(U = 6)$ phase transitions from BOW to CDW.

We can use the two bonds in a unit cell to partition the infinite system into two half-infinite subsystems and compute the von Neumann entanglement entropy $\mathcal{S}_i$. As shown in Fig. 1(b), in the BOW phase, $\mathcal{S}_i$ has different values computed using different partitionings. This corresponds to the spontaneously dimerized phase of the spin chain and the $\mathbb{Z}_2$ degeneracy of the two types of polarization [36,52]. In sharp contrast, the entanglement entropies computed in different ways of partitioning have exactly the same value in the SDW and CDW phases. Therefore, the point where entanglement entropies deviate from one another can be used to locate the BOW phase boundaries, which gives results consistent with those obtained from the two energies.

Sampling. We obtain our emulated experimental data by sampling finite subsystems of the translational invariant states found by VUMPS. To obtain a sample, we repeat the tensors of the unit cell, and sample the resulting subsystem as one would sample a finite MPS [70,71]. More specifically, we

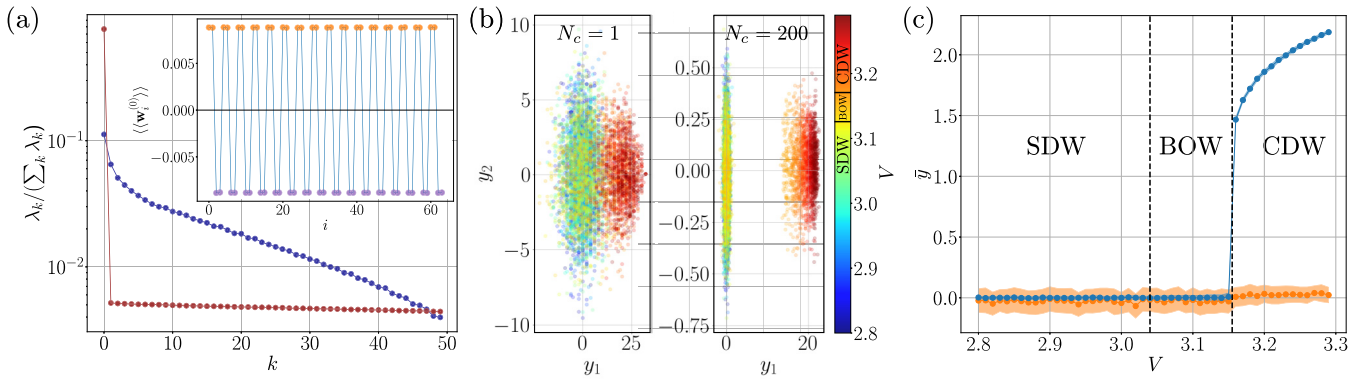

FIG. 2. Principal component analysis of the samples generated at $U = 6$ and different values of $V \in [2.8, 3.3]$ in a uniform grid with separation $\Delta V = 0.1$. (a) The relative weight of the eigenvalues of the covariance matrix for two values of concatenated samples N_c (see [69]). The inset shows the amplitude of the first principal component for $N_c = 200$, averaged over the concatenated samples. (b) Projection of the input features to the first two principal components both when $N_c = 1$ and $N_c = 200$. The color indicates the value of V to which each projected feature belongs. (c) Average projection of the input features corresponding to a fixed V to the first (blue) and second (orange) principal components for $N_c = 200$. The shaded region shows the variance of the average, measuring the spread of the projected input features at a fixed V. Vertical dashed lines indicate the phase transition points obtained form the entanglement entropy.

start by tracing our system down to a single site and sampling from the resulting density matrix, projecting onto the local state that was found and iterating the procedure over the finite subsystem. The unit cell is repeated sixteen times, providing samples that correspond to a chain of length $L = 32$ sites. For each value of U and V, $N_s = 50\,000$ samples are collected. The sampled spin-resolved occupancy is stored in a feature array $\mathbf{x}$ of length $2L$, where even and odd entries represent the spin-up and spin-down occupancy for each lattice site.

Spontaneous Symmetry Breaking Considerations. The states found by VUMPS spontaneously break the $SU(2)$ symmetry of the model, and the spin direction of the state found by VUMPS will depend on details of the optimization, such as the initial state. Therefore, getting multiple samples from the same state obtained by VUMPS can be biased by the arbitrary spin direction of the state. To reduce this effect, we apply a random local $SU(2)$ spin rotation uniformly to each site of the state before we obtain each sample.

While the continuous $SU(2)$ symmetry is restored when producing the samples, the discrete $\mathcal{Z}_2$ symmetry present in BOW and CDW phases is broken in the VUMPS wave function [see Figs. 1(a) and 1(b)]. Even if the experimental procedure does not break the $\mathcal{Z}_2$ symmetry in the CDW phase (the wave function is the homogeneous linear combination of both configurations), each individual sample will reflect which of the two ground states it comes from. There, the symmetry can be explicitly broken by post processing the samples, i.e., by translating by one site those that do not share the same pattern. Furthermore, the use of an even number of lattice sites, together with open boundary conditions (as commonly done in experiments), will break the $\mathcal{Z}_2$ symmetry in the BOW phase. Open boundary conditions effectively provide a pinning field in the kinetic energy, forcing the strong bonds to be adjacent to the edges of the lattice [57] (see [69] for a demonstration using exact diagonalization on chains of finite length). Therefore, the conclusions obtained with our emulated projective measurements are applicable to experimental data without loss of generality.

Principal Component Analysis. Fixing the value of U, we run PCA on samples generated for different values of V to explore fixed-U cuts of the phase diagram. As a dimensional reduction method, PCA projects samples onto directions of largest variance in the data. It has been applied to detect phase transitions based on Monte Carlo samples for classical and quantum models [25,30,32,72].

We find that the spread of the projected samples at fixed V can be reduced, leading to a better resolution, if the input features $\mathbf{x}$ contain N_c concatenated spin-resolved samples. Figure 2(a) shows the relative weight of the eigenvalues of the covariance matrix of data, which represents the variance along the principal components, for samples generated at $U = 6$ and different values of V for $N_c = 1$ and $N_c = 200$. The increase in concatenated features reveals only one relevant principal component. The inset of Fig. 2(a) shows the average of the first principal component, revealing its average action on the spin-resolved occupancy as the π component of the Fourier transform of the total charge distribution. This quantity is the order parameter for the CDW phase.

Figure 2(b) shows the effect of the concatenation of the input features on their projection to the first two principal components. We observe that the first principal component resolves two clusters. The first one corresponding to samples in SDW and the BOW phases, and the second one containing samples from the CDW phase. Figure 2(c) shows, for a fixed value of U and V, the average projection of the input features to the first and second principal components ($N_c = 200$). As expected by the connection of the first principal component with the CDW order parameter, PCA can only resolve the BOW-CDW phase transition and its nature, first or second order (see [69] for the PCA of the samples at different values of U). However, it shows no signal for the BKT-type transition between SDW and BOW phases.

Multiscale Structural Complexity. Recently, the multiscale structural complexity measure [61] has been used to obtain off-diagonal information about quantum states through projective measurements in a single basis [62]. As shown

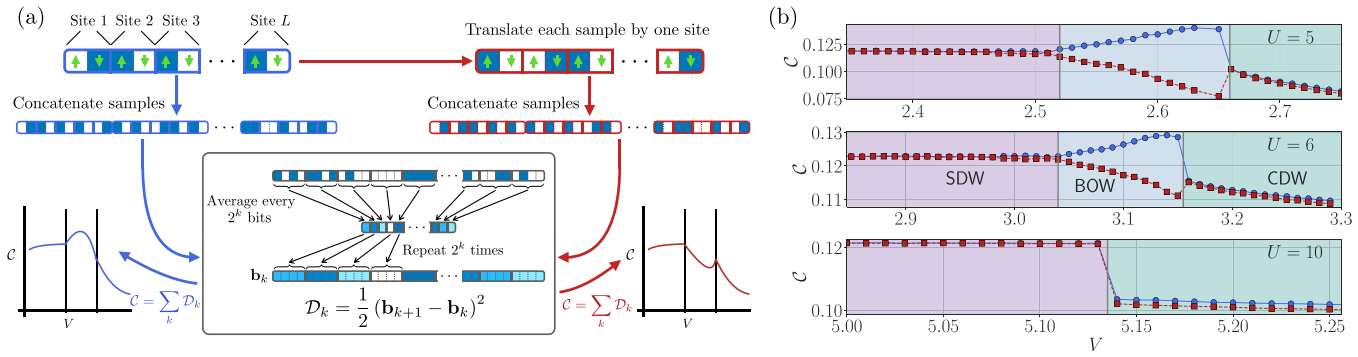

FIG. 3. (a) Procedure for computing the structural complexity. N_s samples are produced for a single ground state for a fixed value of U and V. The samples are then concatenated together, or translated by one lattice site and concatenated together. The multiscale structural complexity is computed for both resulting bitstrings. One coarse-graining step is shown in the box, consisting in the computation of the average of adjacent groups of 2^k bits. (b) Multiscale structural complexity $\mathcal{C}$ as a function of nearest-neighbor interaction V at fixed $U = 5$, $U = 6$, and $U = 10$. The connected blue circles and red squares correspond to the upper and lower branches of the complexity measure in the BOW phase. The two branches are obtained by computing the structural complexity from the samples extracted directly from the emulated ground-state wave function and the samples obtained after translation by one lattice site as shown in panel (a).

schematically in Fig. 3(a), the idea consists of concatenating all available samples for the same quantum state (creating a bitstring), performing several coarse-graining steps, and computing the dissimilarity $\mathcal{D}_k$ between consecutive coarse-graining steps k and $k+1$ [62,69]. These dissimilarities are added, except for the first step, to obtain the so-called multiscale structural complexity $\mathcal{C}$.

For each (U, V) point, the N_s spin-resolved samples are concatenated in two ways: (i) concatenation without shifting and (ii) concatenation after translating all samples by one site (two bits with spin resolution) considering a periodic boundary for the bitstring. These form two sets of bitstrings of length $2 \cdot L \cdot N_s$ each.

As shown in Fig. 3(b), the multiscale structural complexity captures both phase transitions. The two sets of complexity analyses give essentially the same, almost constant, $\mathcal{C}$ (up to a constant shift) inside the SDW phase. As V is increased, the transition to a BOW phase is clearly indicated by the splitting of the complexity measures into two branches. One branch increases as V is increased while the other branch decreases, corresponding to the two types of polarization of strong and weak kinetic energy bonds in the BOW phase. The higher (lower) value of $\mathcal{C}$ is associated with a higher (lower) number of high kinetic energy bonds in the chain of length L. As we keep increasing V, the two branches collapse into a single curve, indicating the transition to the CDW phase. The absence of the BOW phase for $U = 10$ is indicated by the lack of bifurcation of the complexity measure.

It is worth noting that if we generate samples with equal probability from degenerate states in the BOW phase, the complexity does not bifurcate in the BOW phase like it does in Fig. 3(b). This is shown in Supplemental Material [69]. It is then concluded that for the resolution of the BKT-type transition from the complexity analysis of single-basis projective measurements, we need samples that come from only one of the degenerate ground states. As discussed above, this can be achieved by imposing open boundary conditions [57,69] or diagonal edge pinning fields [55,73,74].

Phase Diagram. Figure 1(c) compares the phase boundaries determined by the entanglement entropy $\mathcal{S}_i$ (red triangles) with those determined using the structural complexity $\mathcal{C}$, computed from samples directly (blue squares). The complexity analysis gives accurate results and quantitatively agrees with the off-diagonal observables computed from the wave function in the TDL within error bars. Our results are also consistent with previous works [36,52]. Furthermore, obtaining the ground-state wave function in the TDL and combining local observables with machine learning approaches can shed light on the challenges of quantitatively locating the BKT-type transition [52,53,55–57].

Conclusion. In this work, we use the VUMPS algorithm to generate the 1D ground state wave function of the extended Hubbard model directly in the TDL, which allows us to determine phase boundaries with high precision without considering boundary effects and finite-size scaling. We sample real-space snapshots of finite length and use them along with unsupervised learning methods to characterize the BKT-type phase transition between SDW and BOW phases as well as the first-order and second-order phase transition between BOW and CDW phases. We find that off-diagonal long-range order cannot be detected by the PCA even after concatenation of samples. However, using the structural complexity analysis, the off-diagonal long-range order can be detected using spin-resolved fermion density snapshots if these snapshots are generated from one of the degenerate ground states of the BOW phase. We argue that in optical lattice experiments, this can be achieved by imposing open boundary conditions. Our results indicate the potential of machine learning techniques in revealing microscopic mechanisms and hidden orders using projective measurements of corresponding thermal density matrix in quantum gas microscopes. While detection of phases with off-diagonal long-range order using diagonal descriptors has been demonstrated, further work is required to see if ML methods such as multiscale complexity can also differentiate between BKT and second order transitions from which they emerge. Likewise, it should be noted

that while the structural complexity effectively locates transitions, it does not directly yield the physical nature of the order.

Acknowledgments. We are indebted to A. Millis for carefully reading the manuscript. We would like to thank B. Kloss, A. Sandvik, M. Stoudenmire, S. Trebst, and S. White for insightful discussions. Flatiron Institute is a division of the Simons Foundation. B.X. acknowledge support from the U.S. Department of Energy, Office of Science, National Quantum Information Science Research Centers, Quantum Science Center during the publication process. The work of E.K. and R.S. was supported by the Grant DE-SC-0022311, funded by the US Department of Energy, Office of Science. D.S. was supported by AFOSR Grant FA9550-21-1-0236.

[1] J. F. Sherson, C. Weitenberg, M. Endres, M. Cheneau, I. Bloch, and S. Kuhr, Single-atom-resolved fluorescence imaging of an atomic Mott insulator, Nature (London) **467**, 68 (2010).

[2] W. S. Bakr, A. Peng, M. E. Tai, R. Ma, J. Simon, J. I. Gillen, S. Foelling, L. Pollet, and M. Greiner, Probing the superfluid–to–Mott insulator transition at the single-atom level, Science **329**, 547 (2010).

[3] C. Gross and W. S. Bakr, Quantum gas microscopy for single atom and spin detection, Nat. Phys. **17**, 1316 (2021).

[4] M. F. Parsons, A. Mazurenko, C. S. Chiu, G. Ji, D. Greif, and M. Greiner, Site-resolved measurement of the spin-correlation function in the Fermi-Hubbard model, Science **353**, 1253 (2016).

[5] L. W. Cheuk, M. A. Nichols, K. R. Lawrence, M. Okan, H. Zhang, E. Khatami, N. Trivedi, T. Paiva, M. Rigol, and M. W. Zwierlein, Observation of spatial charge and spin correlations in the 2D Fermi-Hubbard model, Science **353**, 1260 (2016).

[6] P. T. Brown, D. Mitra, E. Guardado-Sanchez, P. Schauß, S. S. Kondov, E. Khatami, T. Paiva, N. Trivedi, D. A. Huse, and W. S. Bakr, Spin-imbalance in a 2D Fermi-Hubbard system, Science **357**, 1385 (2017).

[7] A. Mazurenko, C. S. Chiu, G. Ji, M. F. Parsons, M. Kanász-Nagy, R. Schmidt, F. Grusdt, E. Demler, D. Greif, and M. Greiner, A cold-atom Fermi–Hubbard antiferromagnet, Nature (London) **545**, 462 (2017).

[8] T. Hartke, B. Oreg, C. Turnbaugh, N. Jia, and M. Zwierlein, Direct observation of nonlocal fermion pairing in an attractive Fermi-Hubbard gas, Science **381**, 82 (2023).

[9] P. Schauß, M. Cheneau, M. Endres, T. Fukuhara, S. Hild, A. Omran, T. Pohl, C. Gross, S. Kuhr, and I. Bloch, Observation of spatially ordered structures in a two-dimensional Rydberg gas, Nature (London) **491**, 87 (2012).

[10] S. Ebadi, T. T. Wang, H. Levine, A. Keesling, G. Semeghini, A. Omran, D. Bluvstein, R. Samajdar, H. Pichler, W. W. Ho *et al.*, Quantum phases of matter on a 256-atom programmable quantum simulator, Nature (London) **595**, 227 (2021).

[11] P. Scholl, M. Schuler, H. J. Williams, A. A. Eberharter, D. Barredo, K.-N. Schymik, V. Lienhard, L.-P. Henry, T. C. Lang, T. Lahaye *et al.*, Quantum simulation of 2D antiferromagnets with hundreds of Rydberg atoms, Nature (London) **595**, 233 (2021).

[12] R. Samajdar, W. W. Ho, H. Pichler, M. D. Lukin, and S. Sachdev, Complex density wave orders and quantum phase transitions in a model of square-lattice Rydberg atom arrays, Phys. Rev. Lett. **124**, 103601 (2020).

[13] A. Browaeys and T. Lahaye, Many-body physics with individually controlled Rydberg atoms, Nat. Phys. **16**, 132 (2020).

[14] H. Labuhn, D. Barredo, S. Ravets, S. De Léséleuc, T. Macrì, T. Lahaye, and A. Browaeys, Tunable two-dimensional arrays of single Rydberg atoms for realizing quantum Ising models, Nature (London) **534**, 667 (2016).

[15] H. Bernien, S. Schwartz, A. Keesling, H. Levine, A. Omran, H. Pichler, S. Choi, A. S. Zibrov, M. Endres, M. Greiner *et al.*, Probing many-body dynamics on a 51-atom quantum simulator, Nature (London) **551**, 579 (2017).

[16] P. Mehta, M. Bukov, C.-H. Wang, A. G. Day, C. Richardson, C. K. Fisher, and D. J. Schwab, A high-bias, low-variance introduction to machine learning for physicists, Phys. Rep. **810**, 1 (2019).

[17] G. Carleo, I. Cirac, K. Cranmer, L. Daudet, M. Schuld, N. Tishby, L. Vogt-Maranto, and L. Zdeborová, Machine learning and the physical sciences, Rev. Mod. Phys. **91**, 045002 (2019).

[18] S. Johnston, E. Khatami, and R. Scalettar, A perspective on machine learning and data science for strongly correlated electron problems, Carbon Trends **9**, 100231 (2022).

[19] A. Bohrdt, C. S. Chiu, G. Ji, M. Xu, D. Greif, M. Greiner, E. Demler, F. Grusdt, and M. Knap, Classifying snapshots of the doped Hubbard model with machine learning, Nat. Phys. **15**, 921 (2019).

[20] E. Khatami, E. Guardado-Sanchez, B. M. Spar, J. F. Carrasquilla, W. S. Bakr, and R. T. Scalettar, Visualizing strange metallic correlations in the two-dimensional Fermi-Hubbard model with artificial intelligence, Phys. Rev. A **102**, 033326 (2020).

[21] C. Miles, A. Bohrdt, R. Wu, C. Chiu, M. Xu, G. Ji, M. Greiner, K. Q. Weinberger, E. Demler, and E.-A. Kim, Correlator convolutional neural networks as an interpretable architecture for image-like quantum matter data, Nat. Commun. **12**, 3905 (2021).

[22] C. Miles, R. Samajdar, S. Ebadi, T. T. Wang, H. Pichler, S. Sachdev, M. D. Lukin, M. Greiner, K. Q. Weinberger, and E.-A. Kim, Machine learning discovery of new phases in programmable quantum simulator snapshots, Phys. Rev. Res. **5**, 013026 (2023).

[23] B. S. Rem, N. Käming, M. Tarnowski, L. Asteria, N. Fläschner, C. Becker, K. Sengstock, and C. Weitenberg, Identifying quantum phase transitions using artificial neural networks on experimental data, Nat. Phys. **15**, 917 (2019).

[24] N. Käming, A. Dawid, K. Kottmann, M. Lewenstein, K. Sengstock, A. Dauphin, and C. Weitenberg, Unsupervised machine learning of topological phase transitions from experimental data, Machine Learn.: Sci. Tech. **2**, 035037 (2021).

[25] L. Wang, Discovering phase transitions with unsupervised learning, Phys. Rev. B **94**, 195105 (2016).

[26] J. Carrasquilla and R. G. Melko, Machine learning phases of matter, Nat. Phys. **13**, 431 (2017).

[27] P. Broecker, J. Carrasquilla, R. G. Melko, and S. Trebst, Machine learning quantum phases of matter beyond the fermion sign problem, Sci. Rep. **7**, 8823 (2017).

[28] K. Ch'ng, J. Carrasquilla, R. G. Melko, and E. Khatami, Machine learning phases of strongly correlated fermions, Phys. Rev. X **7**, 031038 (2017).

[29] Y. Zhang and E.-A. Kim, Quantum loop topography for machine learning, Phys. Rev. Lett. **118**, 216401 (2017).

[30] W. Hu, R. R. P. Singh, and R. T. Scalettar, Discovering phases, phase transitions, and crossovers through unsupervised machine learning: A critical examination, Phys. Rev. E **95**, 062122 (2017).

[31] E. P. Van Nieuwenburg, Y.-H. Liu, and S. D. Huber, Learning phase transitions by confusion, Nat. Phys. **13**, 435 (2017).

[32] S. J. Wetzel and M. Scherzer, Machine learning of explicit order parameters: From the Ising model to SU(2) lattice gauge theory, Phys. Rev. B **96**, 184410 (2017).

[33] M. J. S. Beach, A. Golubeva, and R. G. Melko, Machine learning vortices at the Kosterlitz-Thouless transition, Phys. Rev. B **97**, 045207 (2018).

[34] J. F. Rodriguez-Nieva and M. S. Scheurer, Identifying topological order through unsupervised machine learning, Nat. Phys. **15**, 790 (2019).

[35] Y. Miyajima, Y. Murata, Y. Tanaka, and M. Mochizuki, Machine learning detection of Berezinskii-Kosterlitz-Thouless transitions in q-state clock models, Phys. Rev. B **104**, 075114 (2021).

[36] S. Ejima and S. Nishimoto, Phase diagram of the one-dimensional half-filled extended Hubbard model, Phys. Rev. Lett. **99**, 216403 (2007).

[37] T. Ishiguro and K. Yamaji, *Organic Superconductors* (Springer, Berlin, Heidelberg, 1990).

[38] E. Dagotto and T. Rice, Surprises on the way from one-to two-dimensional quantum magnets: the ladder materials, Science **271**, 618 (1996).

[39] J. Hu, T. W. Odom, and C. M. Lieber, Chemistry and physics in one dimension: synthesis and properties of nanowires and nanotubes, Acc. Chem. Res. **32**, 435 (1999).

[40] H. Ishii, H. Kataura, H. Shiozawa, H. Yoshioka, H. Otsubo, Y. Takayama, T. Miyahara, S. Suzuki, Y. Achiba, M. Nakatake *et al.*, Direct observation of Tomonaga–Luttinger-liquid state in carbon nanotubes at low temperatures, Nature (London) **426**, 540 (2003).

[41] S. Baier, M. J. Mark, D. Petter, K. Aikawa, L. Chomaz, Z. Cai, M. Baranov, P. Zoller, and F. Ferlaino, Extended Bose-Hubbard models with ultracold magnetic atoms, Science **352**, 201 (2016).

[42] H. Shiba, Magnetic susceptibility at zero temperature for the one-dimensional Hubbard model, Phys. Rev. B **6**, 930 (1972).

[43] M. Imada and Y. Hatsugai, Numerical studies on the Hubbard model and the t-J model in one-and two-dimensions, J. Phys. Soc. Jpn. **58**, 3752 (1989).

[44] H. J. Schulz, Correlation exponents and the metal-insulator transition in the one-dimensional Hubbard model, Phys. Rev. Lett. **64**, 2831 (1990).

[45] P. Sengupta, A. W. Sandvik, and D. K. Campbell, Bond-order-wave phase and quantum phase transitions in the one-dimensional extended Hubbard model, Phys. Rev. B **65**, 155113 (2002).

[46] R. T. Clay, S. Mazumdar, and D. K. Campbell, Pattern of charge ordering in quasi-one-dimensional organic charge-transfer solids, Phys. Rev. B **67**, 115121 (2003).

[47] F. H. L. Essler, H. Frahm, F. Göhmann, A. Klümper, and V. E. Korepin, *The One-Dimensional Hubbard Model* (Cambridge University Press, Cambridge, UK, 2005).

[48] A. W. Sandvik and D. K. Campbell, Spin-Peierls transition in the Heisenberg chain with finite-frequency phonons, Phys. Rev. Lett. **83**, 195 (1999).

[49] M. Nakamura, Tricritical behavior in the extended Hubbard chains, Phys. Rev. B **61**, 16377 (2000).

[50] M. Tsuchiizu and A. Furusaki, Phase diagram of the one-dimensional extended Hubbard model at half filling, Phys. Rev. Lett. **88**, 056402 (2002).

[51] E. Jeckelmann, Ground-state phase diagram of a half-filled one-dimensional extended Hubbard model, Phys. Rev. Lett. **89**, 236401 (2002).

[52] A. W. Sandvik, L. Balents, and D. K. Campbell, Ground state phases of the half-filled one-dimensional extended Hubbard model, Phys. Rev. Lett. **92**, 236401 (2004).

[53] Y. Z. Zhang, Dimerization in a half-filled one-dimensional extended Hubbard model, Phys. Rev. Lett. **92**, 246404 (2004).

[54] S. Ejima, F. H. L. Essler, F. Lange, and H. Fehske, Ising tricriticality in the extended Hubbard model with bond dimerization, Phys. Rev. B **93**, 235118 (2016).

[55] J. Spalding, S.-W. Tsai, and D. K. Campbell, Critical entanglement for the half-filled extended Hubbard model, Phys. Rev. B **99**, 195445 (2019).

[56] M. Dalmonte, J. Carrasquilla, L. Taddia, E. Ercolessi, and M. Rigol, Gap scaling at Berezinskii-Kosterlitz-Thouless quantum critical points in one-dimensional Hubbard and Heisenberg models, Phys. Rev. B **91**, 165136 (2015).

[57] S. Julià-Farré, D. González-Cuadra, A. Patscheider, M. J. Mark, F. Ferlaino, M. Lewenstein, L. Barbiero, and A. Dauphin, Revealing the topological nature of the bond order wave in a strongly correlated quantum system, Phys. Rev. Res. **4**, L032005 (2022).

[58] V. Zauner-Stauber, L. Vanderstraeten, M. T. Fishman, F. Verstraete, and J. Haegeman, Variational optimization algorithms for uniform matrix product states, Phys. Rev. B **97**, 045145 (2018).

[59] V. Zauner-Stauber, L. Vanderstraeten, J. Haegeman, I. P. McCulloch, and F. Verstraete, Topological nature of spinons and holons: Elementary excitations from matrix product states with conserved symmetries, Phys. Rev. B **97**, 235155 (2018).

[60] L. Vanderstraeten, J. Haegeman, and F. Verstraete, Tangent-space methods for uniform matrix product states, SciPost Phys. Lect. Notes 7 (2019).

[61] A. A. Bagrov, I. A. Iakovlev, A. A. Iliasov, M. I. Katsnelson, and V. V. Mazurenko, Multiscale structural complexity of natural patterns, Proc. Natl. Acad. Sci. USA **117**, 30241 (2020).

[62] O. M. Sotnikov, I. A. Iakovlev, A. A. Iliasov, M. I. Katsnelson, A. A. Bagrov, and V. V. Mazurenko, Certification of quantum states with hidden structure of their bitstrings, npj Quantum Inf. **8**, 41 (2022).

[63] J. Haegeman, J. I. Cirac, T. J. Osborne, I. Pižorn, H. Verschelde, and F. Verstraete, Time-dependent variational principle for quantum lattices, Phys. Rev. Lett. **107**, 070601 (2011).

[64] J. Haegeman, C. Lubich, I. Oseledets, B. Vandereycken, and F. Verstraete, Unifying time evolution and optimization with matrix product states, Phys. Rev. B **94**, 165116 (2016).

[65] I. P. McCulloch, Infinite size density matrix renormalization group, revisited, arXiv:0804.2509.

[66] S. R. White, Density matrix formulation for quantum renormalization groups, Phys. Rev. Lett. **69**, 2863 (1992).

[67] U. Schollwöck, The density-matrix renormalization group, Rev. Mod. Phys. **77**, 259 (2005).

[68] M. Fishman, S. R. White, and E. M. Stoudenmire, The ITensor software library for tensor network calculations, SciPost Phys. Code. 4 (2022).

[69] See Supplemental Material at http://link.aps.org/supplemental/10.1103/PhysRevResearch.6.L022064 for the dependence of correlation length and von Neumann entanglement entropy on bond dimension, a detailed analysis in the weak coupling regime, the effects of mixed polarizations, and the use of open boundary conditions as pinning fields for the experimental proposal, and which includes Refs. [75–79].

[70] S. R. White, Minimally entangled typical quantum states at finite temperature, Phys. Rev. Lett. **102**, 190601 (2009).

[71] E. M. Stoudenmire and S. R. White, Minimally entangled typical thermal state algorithms, New J. Phys. **12**, 055026 (2010).

[72] E. Khatami, Principal component analysis of the magnetic transition in the three-dimensional Fermi-Hubbard model, J. Phys.: Conf. Ser. **1290**, 012006 (2019).

[73] F. F. Assaad and I. F. Herbut, Pinning the order: The nature of quantum criticality in the Hubbard model on honeycomb lattice, Phys. Rev. X **3**, 031010 (2013).

[74] B. Xiao, Y.-Y. He, A. Georges, and S. Zhang, Temperature dependence of spin and charge orders in the doped two-dimensional hubbard model, Phys. Rev. X **13**, 011007 (2023).

[75] R. Orús, A practical introduction to tensor networks: Matrix product states and projected entangled pair states, Ann. Phys. **349**, 117 (2014).

[76] M. M. Rams, P. Czarnik, and L. Cincio, Precise extrapolation of the correlation function asymptotics in uniform tensor network states with application to the Bose-Hubbard and XXZ models, Phys. Rev. X **8**, 041033 (2018).

[77] L. Tagliacozzo, T. R. de Oliveira, S. Iblisdir, and J. I. Latorre, Scaling of entanglement support for matrix product states, Phys. Rev. B **78**, 024410 (2008).

[78] F. Pollmann, S. Mukerjee, A. M. Turner, and J. E. Moore, Theory of finite-entanglement scaling at one-dimensional quantum critical points, Phys. Rev. Lett. **102**, 255701 (2009).

[79] B. Pirvu, G. Vidal, F. Verstraete, and L. Tagliacozzo, Matrix product states for critical spin chains: Finite-size versus finite-entanglement scaling, Phys. Rev. B **86**, 075117 (2012).